metals

MDPI

Article

Effect of Post-Weld Heat Treatment on Microstructure and Mechanical Properties of Friction-Stir-Welded Al–Cu–Li Alloy

Ben Lin [1,2,3], Ying Li [1,4,*], Xiwu Li [1,2,4], Yongan Zhang [1,2,4,*], Kai Wen [1,2,4], Changlin Li [1,4], Lizhen Yan [1,2,4], Yanan Li [1,2,4], Hongwei Yan [1,2,4], Zhihui Li [1,2] and Baiqing Xiong [1,2]

[1] State Key Laboratory of Nonferrous Structural Materials, China GRINM Group Co., Ltd., Beijing 100088, China; lixiwu@grinm.com (X.L.)
[2] General Research Institute for Nonferrous Metals, Beijing 100088, China
[3] China Academy of Launch Vehicle Technology, Beijing 100076, China
[4] GRIMAT Engineering Institute Co., Ltd., Beijing 101407, China
* Correspondence: liying@grinm.com (Y.L.); zhangyongan@grinm.com (Y.Z.)

Abstract

To address the insufficient strength of friction-stir-welded (FSW) ultra-high-strength Al–Cu–Li alloy joints, the effects of post-weld heat treatment (PWHT) on microstructural evolution and mechanical properties were systematically investigated. The as-welded joint showed a "W"-shaped microhardness profile, with the minimum value located in the thermo-mechanically affected zone (TMAZ), mainly caused by the dissolution of T_1 phases and precipitation of coarse AlCu, AlCuMg, and AlCuMn phases during welding. Direct artificial aging at 155 °C for 24 h failed to improve joint strength due to solute depletion induced by pre-existing coarse secondary phases. Solution treatment re-dissolved coarse precipitates into the matrix, and subsequent aging led to uniform precipitation dominated by T_1 and θ' phases, with a consistent microhardness of ~155 HV across all zones. By introducing pre-stretching deformation after solution treatment, T_1 became the dominant strengthening phase in all regions, accompanied by a remarkable increase in both microhardness and tensile strength. With 3% pre-stretching, the microhardness reached 185 HV, and the ultimate tensile strength of the joint reached 600 MPa, corresponding to a joint efficiency as high as 95%, which is superior to most reported values for Al–Li alloy FSW joints. This study clarifies the precipitation evolution mechanism under tailored PWHT and provides an effective strategy for property regulation of high-performance Al–Cu–Li alloy FSW structures in aerospace applications.

Keywords: Al–Cu–Li alloy; friction stir welding; post-weld heat treatment; precipitation evolution; mechanical properties

Check for updates

Academic Editor: Dariusz Rozumek

Received: 9 April 2026
Revised: 6 May 2026
Accepted: 14 May 2026
Published: 20 May 2026

Copyright: © 2026 by the authors. Licensee MDPI, Basel, Switzerland. This article is an open access article distributed under the terms and conditions of the Creative Commons Attribution (CC BY) license.

1. Introduction

Structural weight reduction is a key technological strategy in the aerospace industry for improving payload capacity, reducing launch costs, and extending operational range [1–3]. Estimates indicate that a reduction in just 1 kg in the structural mass of a launch vehicle or spacecraft can generate economic benefits amounting to tens of thousands of US dollars. Therefore, the development and application of materials with high specific strength and high specific stiffness have consistently been central to spacecraft structural design [2,4]. Al–Li alloys offer exceptional comprehensive properties. Compared with conventional aluminum alloys, each 1% addition of lithium reduces density by approximately 3% while increasing elastic modulus by about 6% [5,6]. These alloys also exhibit good corrosion

resistance and low-temperature toughness [7–9]. As a result, they have emerged as the preferred material for next-generation launch vehicle propellant tanks. In recent years, with the maturation of composition optimization and fabrication processes for third-generation Al–Li alloys (e.g., 2195, 2050, 2060), their use in large-scale thin-walled aerospace structures has increased significantly [7,10,11].

Welding is a key technology in the fabrication of Al-Li alloy components. When conventional fusion welding methods such as tungsten inert gas (TIG) welding and laser welding are used to join Al–Li alloys, several challenges arise due to the highly reactive nature of Li [12,13]. At elevated welding temperatures, Li readily reacts with hydrogen, oxygen, and nitrogen, leading to the formation of pores and oxide inclusions in the weld [14,15]. In addition, Al–Li alloys exhibit high susceptibility to hot cracking, making them prone to solidification cracks in the weld center and heat-affected zone during fusion welding solidification [16]. Furthermore, the substantial heat input characteristic of fusion welding severely degrades the rolled microstructure of the base material, causing coarsening or dissolution of strengthening phases such as T_1 (Al_2CuLi) and δ' (Al_3Li) [17]. As a result, joint efficiency—defined as the ratio of joint strength to base material strength—typically reaches only 60–70%, making it difficult to meet the stringent reliability requirements of aerospace structural design [18].

Friction stir welding (FSW), as a solid-state joining technology, offers a revolutionary solution to the weldability challenges of Al–Li alloys [19]. During FSW, the heat input is relatively low and no melting occurs, which fundamentally avoids common fusion welding defects such as porosity and hot cracking [20]. Moreover, the intense plastic flow and dynamic recrystallization behavior inherent to FSW lead to the formation of fine equiaxed grains in the weld zone [21,22], enabling joints with mechanical properties approaching or even exceeding those of the base material. Consequently, extensive research has been conducted on the FSW of Al–Li alloys by scholars worldwide [23]. Existing studies indicate that optimizing process parameters—such as rotational speed, welding speed, and plunge depth—can effectively suppress defects like the "S" line, grooves, and tunnels in the joint [24]. For example, researchers have reported, that for the 2195 Al–Li alloy, under appropriate welding parameters, joint efficiency can exceed 75% [25].

However, FSW is a non-steady-state process characterized by intense plastic deformation and a complex thermal cycle. The thermo-mechanical coupling effects introduced during welding cause varying degrees of dissolution, reprecipitation, or coarsening of the precipitates in the base material, thereby affecting joint performance [26–28]. For age-hardened Al–Li alloys, the thermal cycle during welding leads to the dissolution of strengthening phases or over-aging softening in the stir zone (SZ) and the thermo-mechanically affected zone (TMAZ), while the heat-affected zone (HAZ) exhibits a distinct softened region [29–31]. Such microstructural heterogeneity limits further improvement in the overall mechanical properties of the joint.

To optimize the mechanical properties of FSW joints, post-weld heat treatment (PWHT) is regarded as a key strengthening strategy. By employing solution treatment to re-dissolve the precipitates followed by aging treatment to achieve controlled reprecipitation, it is theoretically possible to eliminate the microstructural heterogeneity induced by the welding thermal cycle, and even enable the distribution of strengthening phases in the weld zone to exceed that of the original base material [32,33]. Although several studies [34,35] have reported the effects of PWHT on the properties of FSW joints in Al–Li alloys, certain research gaps remain. How to further improve the strength of welded joints by tailoring PWHT parameters remains a critical challenge for engineering applications.

In light of the above, this study systematically investigates the precipitate characteristics in different zones of friction-stir-welded joints of a novel high-strength Al–Li alloy

under various PWHT conditions, and their influence on mechanical properties. The focus is on elucidating the intrinsic relationship among the initial as-welded microstructure, heat treatment parameters, precipitation behavior of strengthening phases, and resulting mechanical properties. The aim is to reveal the microstructural mechanisms underlying the homogenization and property enhancement of FSW joints in Al–Li alloys through PWHT, thereby providing theoretical guidance and experimental data to support the optimization of post-weld processing for aerospace structural components made of Al–Li alloys.

2. Materials and Experiments

2.1. Materials and FSW Process

This study used a 10 mm thick Al–Cu–Li alloy plate in a T8 state as the base material (BM). The chemical composition and mechanical properties of this alloy are shown in Table 1. Before the FSW process, all the plates were cleaned using ethanol. During the FSW process, the optimal FSW parameters with 500 r/min rotation speed and 100 mm/min welding speed were used for welding. The schematic diagrams of the FSW process and the welding tool used in this study are shown in Figure 1a,b. The welding was performed with a plunge depth of 0.2 mm, a tool tilt angle of 2.5°, and a dwell time of 10 s. After the FSW process, the microhardness, tensile properties and microstructures of the joints were tested in the as-welded state and heat-treated states. The heat-treated states included artificial aging (AA) treatment in 155 °C/24 h, solution treatment (ST, 515 °C/2 h) + artificial aging (AA, 155 °C/24 h), and solution treatment (ST, 515 °C/2 h) + pre-stretching deformation (PD, 1.5% and 3%) + artificial aging (AA, 155 °C/24 h). Specimens for pre-stretching were cut perpendicular to the welding direction (parallel to the rolling direction of the plate). Pre-stretching was performed at room temperature on a CMT5105 universal testing machine (SUNS, Shenzhen, China) at a constant crosshead speed of 3 mm/min. And the test was terminated when the total strain of the specimen reached 3%.

Table 1. Chemical composition and mechanical properties of the Al-Cu-Li alloy used in this study.

Chemical Composition, wt.%								Mechanical Properties	
Cu	Li	Mg	Ag	Zn	Mn	Zr	Al	Tensile strength, MPa	Elongation, %
4.00	1.30	0.40	0.40	0.40	0.30	0.10	Bal.	630	9.5

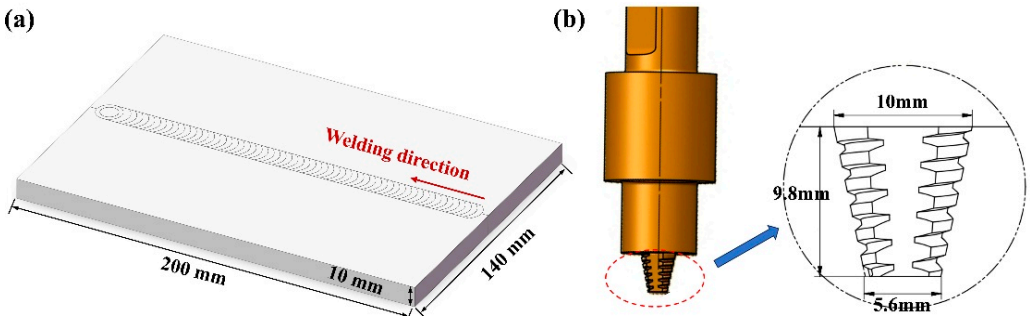


Figure 1. Schematic of the welding process and diagram of welding tool: (**a**) schematic diagram of welding; (**b**) the structure of the welding tool.

2.2. Microhardness and Tensile Test

Microhardness tests were conducted in accordance with ASTM E384-22 [36]. Vickers microhardness measurements of joint cross-sections under the as-welded and heat-treated conditions were carried out using a Buehler Wilson VH1150 tester (Lake Bluff, IL, USA) under an applied load of 5 kg and a spacing of 1 mm between adjacent indentations.

Tensile tests were conducted following ASTM E8-04 [37]. Tensile specimens were machined from the welded joints perpendicular to the welding direction. The tensile properties of joints in the as-welded and heat-treated states were measured at room temperature on a CMT5105 universal testing machine (SUNS, Shenzhen, China) at a constant crosshead speed of 2 mm/min. All tests were repeated three times to reduce experimental error.

2.3. Microstructural Observations

Microstructures including fractography and precipitate features in different regions of the joints were observed using an optical microscope (OM, Leica-DMi8C, Wetzlar, Germany), scanning electron microscope (SEM, JSM-7900F, JEOL Ltd., Tokyo, Japan) and transmission electron microscopy (TEM, Talos F200X, Thermo Fisher Scientific, Waltham, MA, USA). A fractograph of the fracture surface was conducted using SEM. The characteristics of the precipitates were explored using TEM combined with energy-dispersive X-ray spectroscopy (EDS). The TEM samples were electropolished using a twin-jet system with a solution of 25% nitric acid in methanol at −30 °C to −20 °C and an applied voltage of 15–20 V.

3. Results

3.1. Microhardness

Figure 2 presents the microhardness distribution on a cross-section of the as-welded and heat-treated joints. In the as-welded state, the microhardness profile of the welded joint exhibited a "W" shape. The BM zone shows the highest microhardness, with an average value of 200 HV. The stir zone (SZ) has an average microhardness of 140 HV. The lowest microhardness, measured at 110 HV, was found in the thermo-mechanically affected zone (TMAZ) located 10 mm from the weld center. After artificial aging (AA) treatment in 155 °C/24 h, the microhardness distribution across the joint remained in a "W" shape, showing no significant change compared to the as-welded condition. After solution (515 °C/2 h) and artificial aging (155 °C/24 h) treatment (ST + AA), the difference in microhardness between the various regions of the joint was minimal, with all regions exhibiting a microhardness value of approximately 155 HV. Compared to the as-welded state, the microhardness of the SZ, TMAZ, and the heat-affected zone (HAZ) near the SZ increased after ST + AA treatment. Among these, the TMAZ showed the most significant increase, with microhardness improving by approximately 45 HV. Conversely, the microhardness of BM and the HAZ near the BM decreased. To further enhance the mechanical properties across the different regions of the welded joint, pre-stretching deformation was introduced after solution treatment to increase dislocation density and promote subsequent aging precipitation. When the pre-stretching deformation was 1.5%, the microhardness of all joint zones increased to 175 HV. With a pre-stretching deformation of 3%, the microhardness of all joint zones further increased to 185 HV. Introducing pre-stretching deformation after solution treatment significantly improved the microhardness of the welded joint.

3.2. Tensile Properties

Figure 3a presents the tensile properties of the welded joints in both the as-welded and heat-treated conditions. The as-welded joint exhibited an average yield strength (YS) of 300 MPa, an ultimate tensile strength (UTS) of 429 MPa, and an elongation (El) of 5.00%. Following artificial aging (AA) treatment at 155 °C for 24 h, the UTS of the joint did not show a significant increase. To enhance joint strength, a solution + aging treatment was applied. After solution treatment (ST, 515 °C/2 h) followed by aging (AA, 155 °C/24 h), the YS, UTS, and El of the welded joint increased to 401 MPa, 504 MPa, and 7.37%, respectively. In a further effort to improve the joint strength, pre-stretching deformation was introduced after

the solution treatment but before the aging process. When a pre-stretching deformation of 3% was applied, the YS and UTS of the joint were significantly enhanced to 589 MPa and 600 MPa, respectively. The tensile efficiency of the welded joint reached up to 95%.

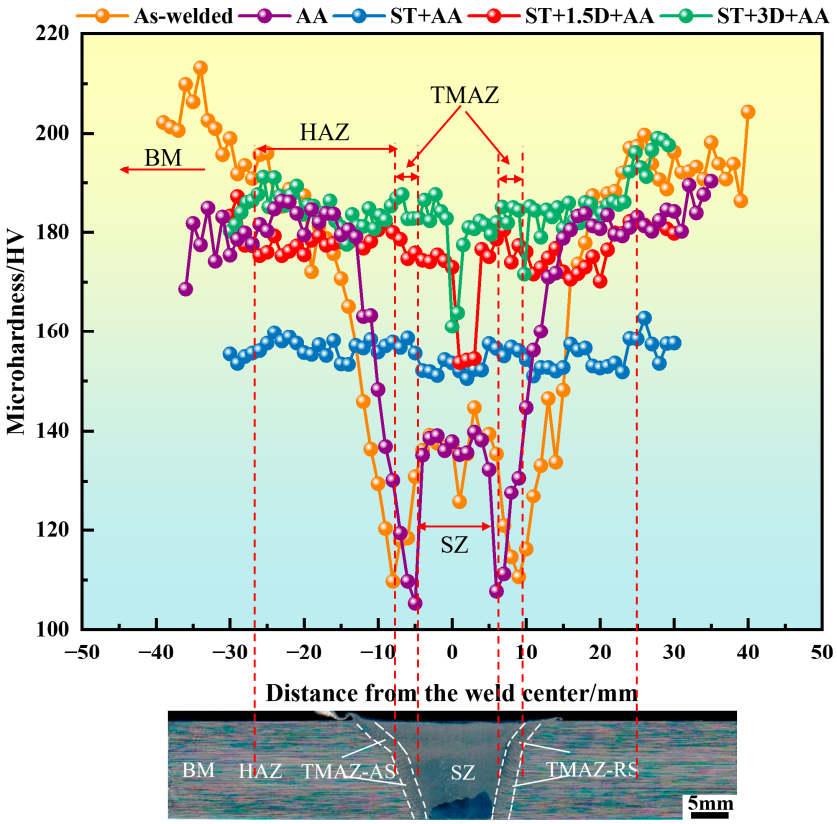


Figure 2. Microhardness profiles of the as-welded and heat-treated joints.

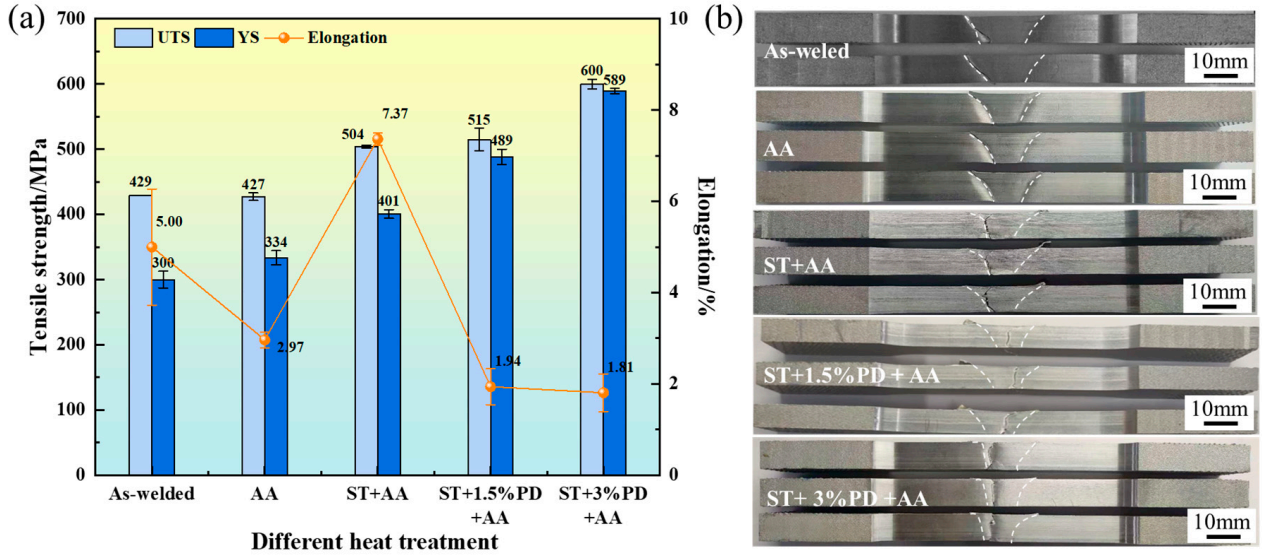


Figure 3. Tensile properties of the as-welded and heat-treated joints: (**a**) the yield strength, ultimate tensile strength, and elongation of the joints; (**b**) macrographs of the fractured tensile samples.

Figure 3b presents the macrographs of the fractured tensile samples from the as-welded and heat-treated joints. It was observed that both the as-welded and AA joints fractured in the TMAZ, with the fracture location corresponding to the region of low microhardness. For the welded joints that underwent solution treatment + pre-stretching deformation + aging (ST + PD +AA), all tensile specimens fractured in the SZ.

Figure 4 shows the fracture features of the typical specimens treated with ST + PD + AA. SEM fractography revealed that, after the solution treatment, a coarse grain layer formed on the upper and lower surfaces of the SZ. Additionally, distinct oxide particles were observed in the SZ. The presence of this coarse grain layer and the oxide particles in the stir zone may be the main reasons for the fracture of the tensile specimens in the SZ after the solution treatment.

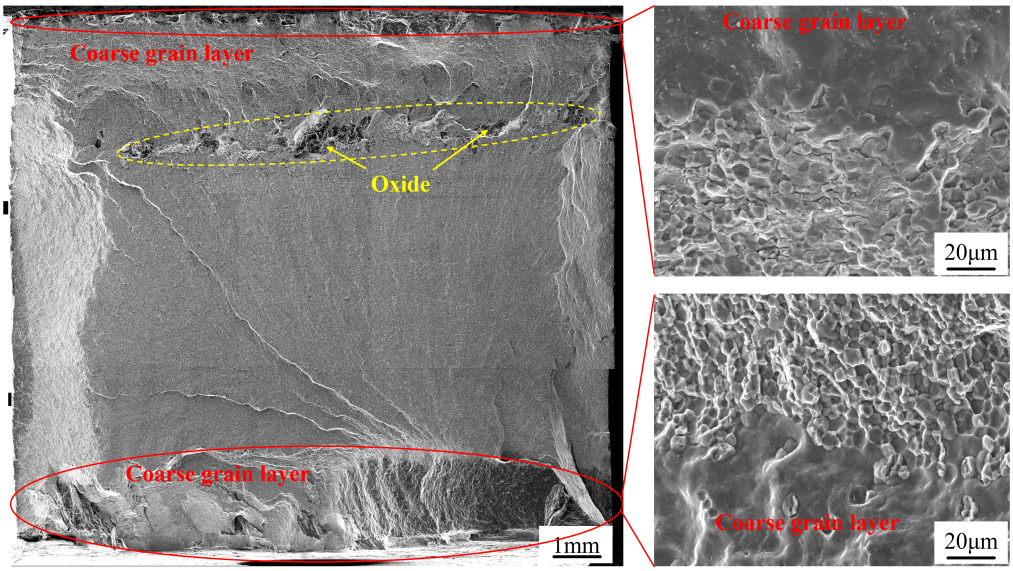


Figure 4. SEM images of the fracture of the typical tensile sample of the welded joint.

3.3. Microstructure

Figure 5a,b presents macrographs of a cross-section of the welded joints in the as-welded and ST + PD + AA states, respectively. Macroscopic observation revealed that, after the solution treatment, abnormal grain growth (AGG) occurred at both the top and bottom of the SZ. In terms of the formation mechanism of AGG in the SZ, previous studies [38] have shown that the extreme surface layer of the SZ experiences the highest temperature and maximum strain during welding, resulting in refined grains that provide a large driving force for recrystallization and grain growth. Meanwhile, this region contains a high density of substructures, making it prone to AGG at elevated temperatures. At the bottom of the SZ, heat dissipation from the base plate during the FSW process, fine grains, and the density of substructures are second only to that of the surface layer, leading to low thermal stability. Consequently, AGG occurs after high-temperature solution treatment.

Metallographic observations were conducted on the "S" line features in the top, middle, and bottom regions of the SZ for the joint subjected to ST + PD + AA treatment (as shown in Figure 5c–e). These features were compared with those in the as-welded joint (shown in Figure 5f–h). It was found that, compared to the as-welded joint, the "S" line characteristics in the SZ became more severe after the high-temperature solution treatment.

The precipitate characteristics constitute a critical factor governing the properties of heat-treatable strengthened aluminum alloys. TEM specimens were extracted from the BM, HAZ, TMAZ and SZ based on the microhardness distribution profile, revealing the variation in mechanical properties across different regions of the joint. These specimens were employed to examine the precipitate features in each zone. Figure 6 presents TEM bright-field images of the grain boundaries and intragranular precipitates in the various regions of the as-welded joint, while Table 2 summarizes the corresponding compositional analysis results. Combined with the compositional analysis, it can be observed that, in the BM and HAZ, nearly continuously distributed AlCu or AlCuMgAg phases were

present along the grain boundaries. Within the grains, a limited number of coarse AlCuMn phases and a high density of T_1 phases were observed. In the TMAZ, coarse AlCu phases proliferated on the grain boundaries, and the grains contained a substantial number of coarse AlCu phases along with a small amount of T_1 phases. In the SZ, coarse AlCuMg phases were found at the grain boundaries, and a considerable quantity of AlCu and AlCuMn phases was precipitated within the grains.

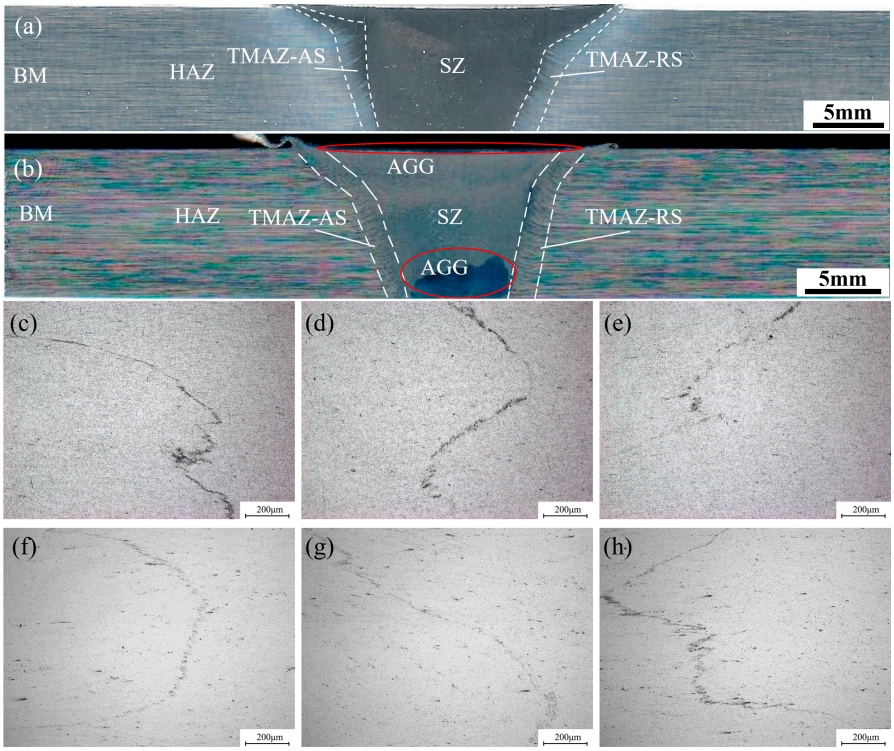


Figure 5. Macrographs and OM images of a cross-section of the as-welded and heat-treated joints: (**a**) macrograph of the as-welded joint; (**b**) macrograph of the heat-treated joint; (**c**–**e**) OM images of the "S" line from the top, middle, and bottom regions of the stir zone in the heat-treated state; (**f**–**h**) OM images of the "S" line from the top, middle, and bottom regions of the stir zone in the as-welded state.

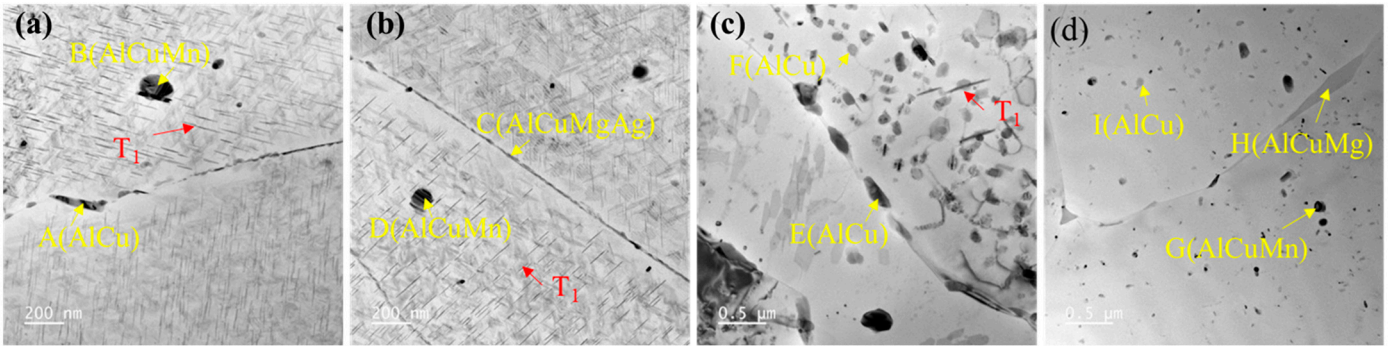


Figure 6. Bright-field TEM images of grain boundary and intragranular precipitates in various zones of the welded joint: (**a**) BM, (**b**) HAZ, (**c**) TMAZ, (**d**) SZ.

TEM analysis was further performed to characterize the nano-scale intragranular precipitates in different regions of the welded joint. Figure 7 presents TEM dark-field images and corresponding compositional spectra of the nano-scale intragranular precipitates in various regions of the as-welded joint, observed along the $<110>_{Al}$ and $<100>_{Al}$ directions, respectively. The statistic results of precipitates revealed that the primary strengthening precipitates within the grains of the BM are T_1 phases, present in high densities and fine

sizes. In the HAZ, the dominant strengthening precipitates remained T_1 phases; however, their size was slightly larger and the average number density was lower compared to those in the BM. In the TMAZ, the density of nano-scale T_1 phases was significantly reduced relative to the BM, with only a limited number of coarse T_1 phases and AlCu phases observed in the grains. In the SZ, the intragranular precipitates consisted predominantly of coarse AlCu and AlCuMn phases, with no appreciable nano-scale T_1 phases detected.

Table 2. EDS results of the precipitates at grain boundaries and within grains in various regions of the as-welded joint (at.%).

Position	Al	Cu	Mg	Ag	Mn	Ti	Zr	Phase
A	67.58	31.85	0.08	0.08	0.05	0.05	0.32	AlCu
B	74.31	11.24	0.15	0.23	13.81	0.04	0.21	AlCuMn
C	69.99	18.01	7.65	3.41	0.16	0.08	0.70	AlCuMgAg
D	80.16	8.54	1.26	0.40	9.19	0.09	0.37	AlCuMn
E	90.56	8.48	0.60	0.23	-	0.02	0.10	AlCu
F	94.71	3.86	0.88	0.30	-	0.03	0.21	AlCu
G	82.85	6.95	0.17	0.21	9.55	0.06	0.20	AlCuMn
H	87.76	6.21	4.51	1.09	0.08	0.06	0.29	AlCuMg
I	92.95	5.37	0.23	0.98	0.07	0.08	0.32	AlCu

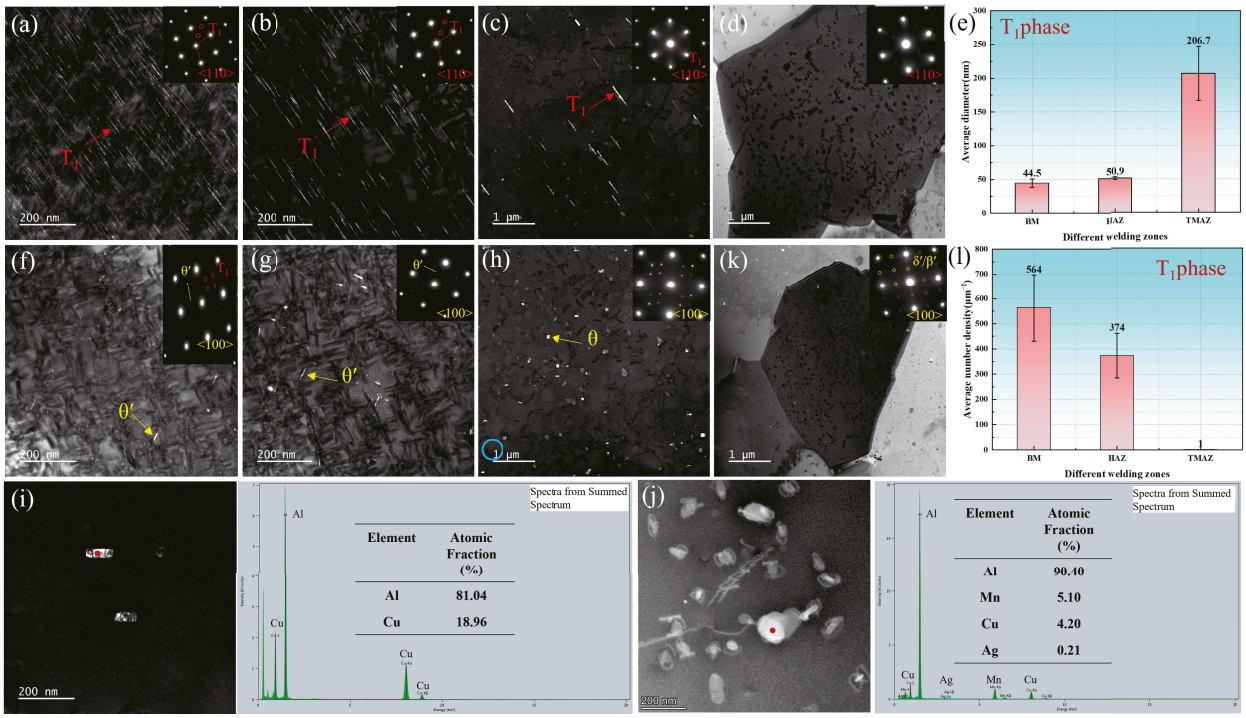


Figure 7. Dark-field TEM images, EDS, and statistic results of precipitates in various regions of the welded joint: (**a**–**d**) TEM images observed along <110>$_{Al}$ zone axis, (**f**–**j**) TEM images observed along <100>$_{Al}$ zone axis, (**a**,**f**) BM, (**b**,**g**) HAZ, (**c**,**h**) TMAZ, (**d**,**k**) SZ, (**e**) average diameter of T_1 phase, (**j**) average number density of T_1 phase, (**k**) EDS analysis spectrum of precipitates in the region highlighted by the blue circle in (**h**), (**l**) EDS analysis spectrum of precipitates in SZ.

To investigate the effect of post-weld heat treatment on the precipitate characteristics in various regions of the welded joint, TEM observations were performed on the different regions of the joint subjected to AA and ST + PD (with deformation amounts of 0%, 1.5%, and 3%, respectively) + AA treatments. Figure 8 presents TEM dark-field images and statistic results of the intragranular precipitates in different regions of the welded joint after AA treatment. The precipitate characteristics in the BM and HAZ did not differ

significantly from those in the as-welded joint, remaining dominated by T_1 phases, along with the precipitation of a small amount of θ′ and S′ phases within the grains. In the TMAZ, the precipitates consisted mainly of coarse T_1 and θ′ phases. Compared with the precipitate characteristics in the TMAZ of the as-welded joint, coarsening of the T_1 and θ′ phases occurred after AA treatment. Following AA treatment, a small number of T_1 phases and a substantial number of θ′ phases were precipitated in the SZ.

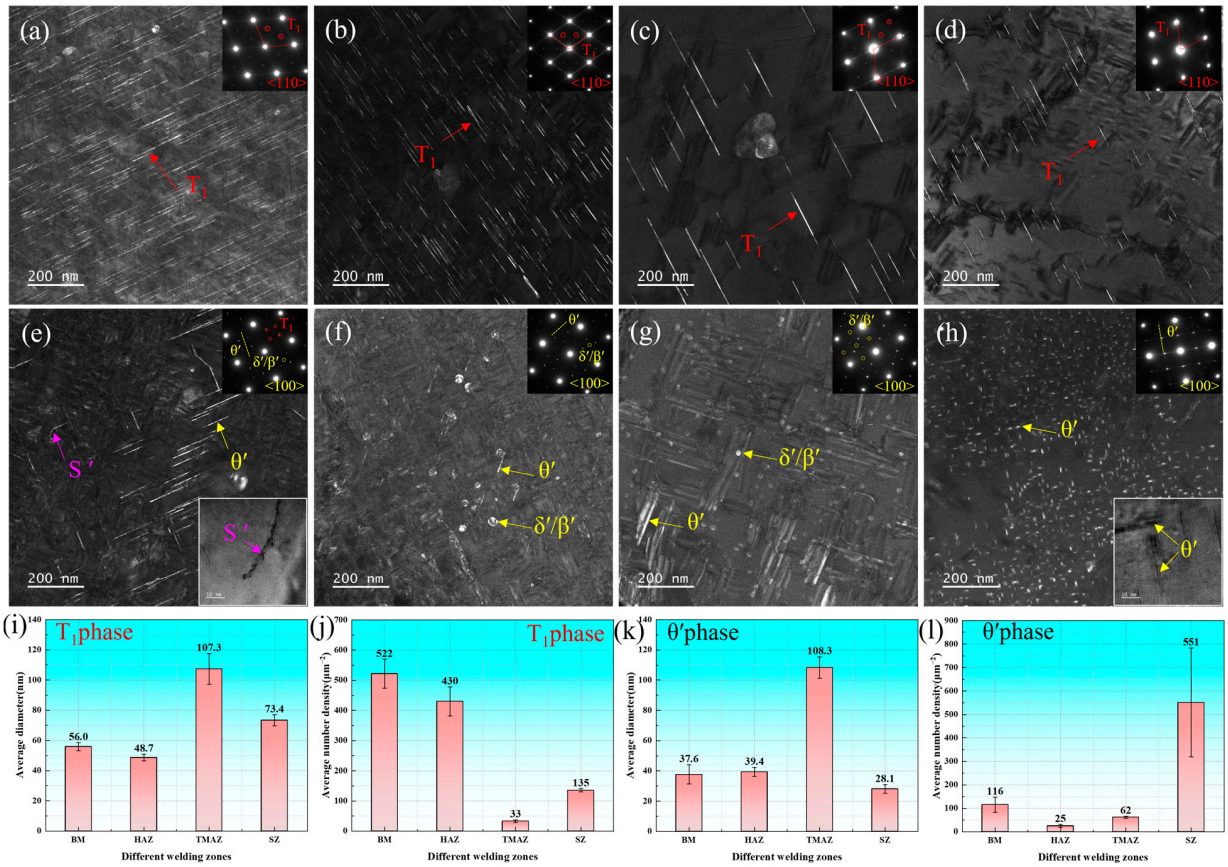


Figure 8. Dark-field TEM images and statistic results of precipitates within grains in various regions of the aging treatment joint: (**a**–**d**) TEM images observed along <110>$_{Al}$ zone axis, (**e**–**h**) TEM images observed along <100>$_{Al}$ zone axis, (**a**,**e**) BM, (**b**,**f**) HAZ, (**c**,**g**) TMAZ, (**d**,**h**) SZ, (**i**) average diameter of T_1 phase, (**j**) average number density of T_1 phase, (**k**) average diameter of θ′ phase, (**l**) average number density of θ′ phase.

Figure 9 shows TEM bright-field images of grain boundary and intragranular precipitates in different regions of the welded joint after ST + AA treatment. Following this treatment, the grain boundary precipitates in all regions of the joint were identified as AlCu or AlCuMgAg phases, along with a small number of AlCuMn phases within the grains. In contrast to the as-welded joint, no significant difference was observed in the large-sized precipitates at grain boundaries and within grains of the BM and HAZ. Notably, the coarse AlCu and AlCuMn phases that had precipitated in the HAZ and SZ of the as-welded joint were largely dissolved back into the matrix after the re-solution treatment.

Figure 10 displays dark-field TEM and HRTEM images, along with statistical results of nano-scale precipitates in different regions of the welded joint after ST + AA treatment. T_1 and θ′ phases act as the dominant strengthening precipitates in the BM, HAZ, TMAZ, and SZ, accompanied by a small amount of S′ (Al_2CuMg) and σ ($Al_5Cu_6Mg_2$) phases. Statistical analyses of T_1 and θ′ precipitates reveal that T_1 phases in the HAZ are slightly larger and more numerous. In comparison, θ′ precipitates in the SZ exhibit a finer size and higher number density.

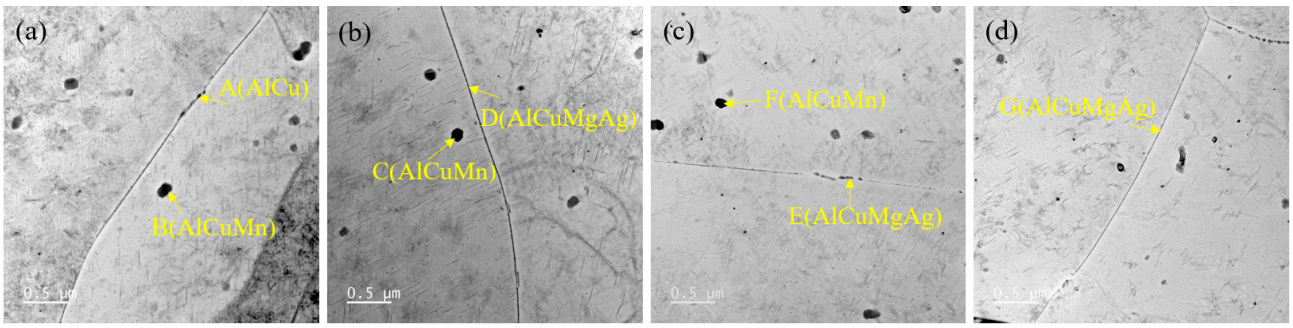


Figure 9. Bright-field TEM images of precipitates at grain boundaries and within grains in various regions of the joint that underwent solid solution and aging treatment: (**a**) BM, (**b**) HAZ, (**c**) TMAZ, and (**d**) SZ.

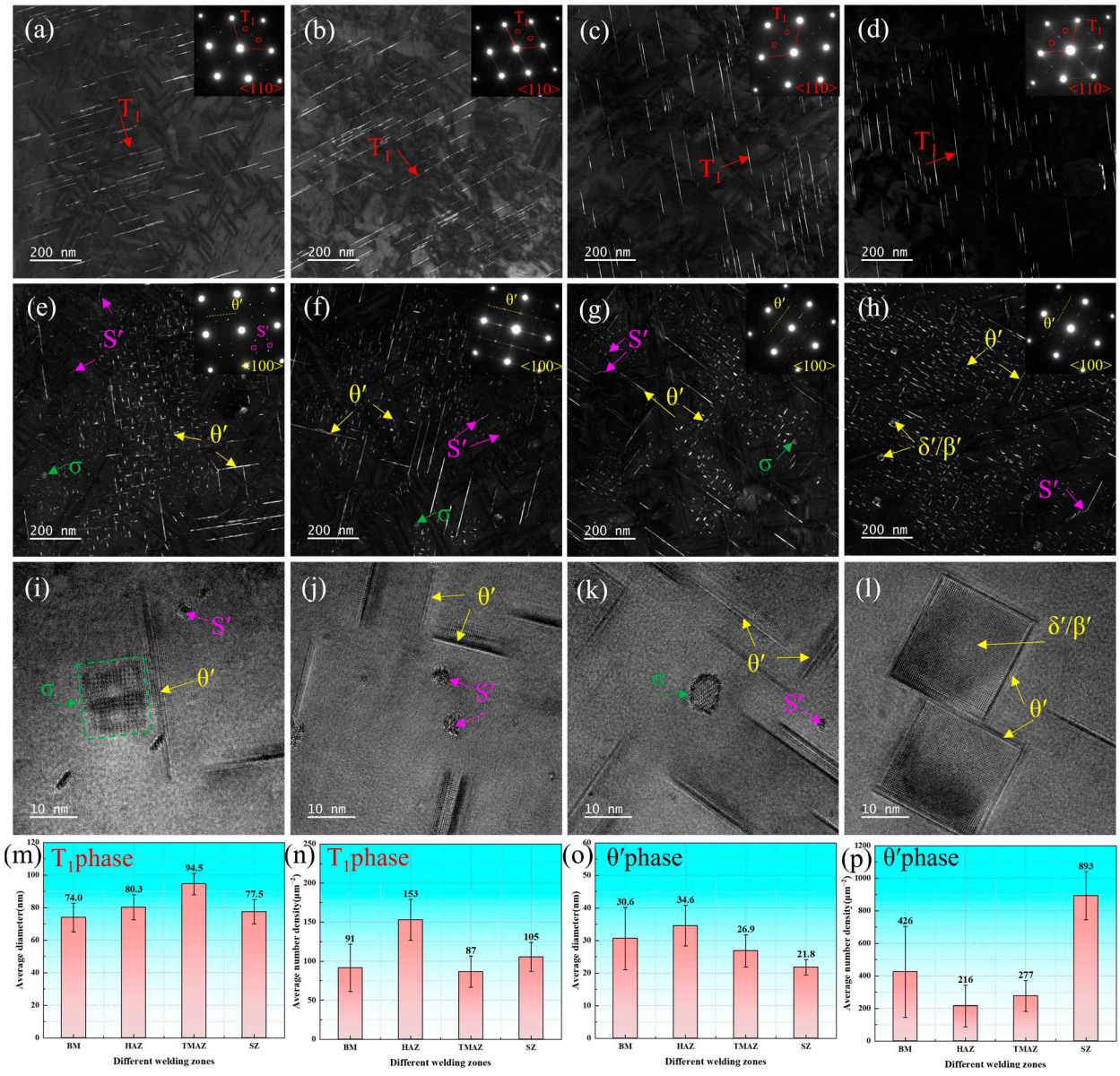


Figure 10. Dark-field TEM and HRTEM images of precipitates within grains in various regions of the joint that underwent solid solution and aging treatment: (**a**–**d**) TEM images observed along <110>$_{Al}$ zone axis, (**e**–**h**) TEM images observed along <100>$_{Al}$ zone axis, (**i**–**l**) HRTEM images, (**a**) BM, (**b**) HAZ, (**c**) TMAZ, (**d**) SZ, (**m**) average diameter of T_1 phase, (**n**) average number density of T_1 phase, (**o**) average diameter of θ′ phase, (**p**) average number density of θ′ phase.

Figure 11 displays dark-field TEM images and statistic results of the precipitates in different regions of the welded joint after ST + 3%PD +AA treatment. After applying 3% pre-stretching deformation prior to aging, the precipitates in the BM, HAZ, TMAZ, and SZ were predominantly T_1 phases, along with a small number of θ′ and S′ phases within the grains. The number density of T_1 phases in the HAZ, TMAZ and SZ was slightly higher than that in BM. Compared with the welded joint without pre-stretching deformation, the application of pre-stretching resulted in a notably higher density of T_1 phases and a marked reduction in the number of θ′ phases.

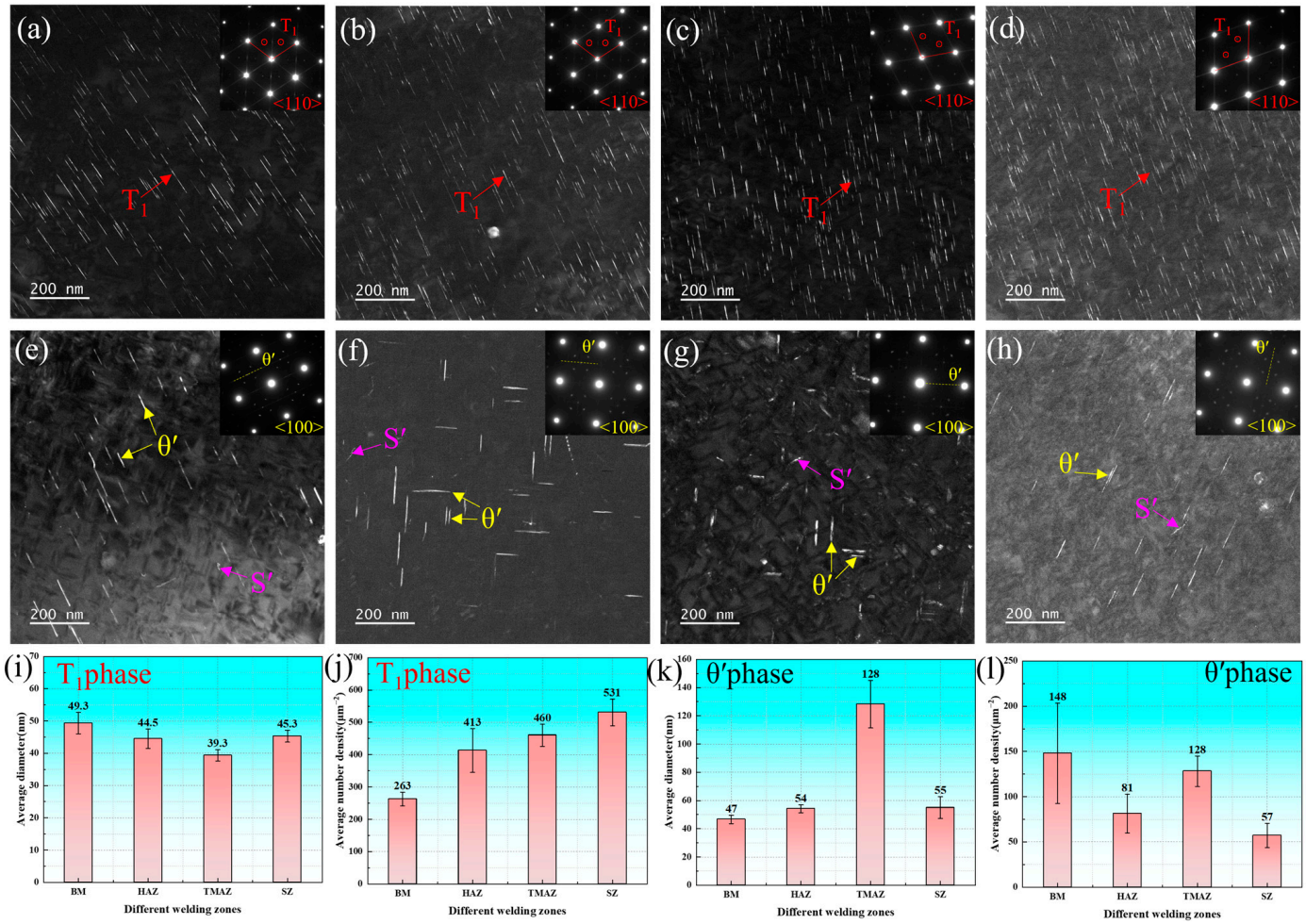


Figure 11. Dark-field TEM images of precipitates within grains in various regions of the joint that underwent ST + 3%PD +AA treatment: (**a**–**d**) TEM images observed along <110>$_{Al}$ zone axis, (**e**–**h**) TEM images observed along <100>$_{Al}$ zone axis, (**a**,**e**) BM, (**b**,**f**) HAZ, (**c**,**g**) TMAZ, (**d**,**h**) SZ, (**i**) average diameter of T_1 phase, (**j**) average number density of T_1 phase, (**k**) average diameter of θ′ phase, (**l**) average number density of θ′ phase.

4. Discussion

The novel Al–Cu–Li alloy is a heat-treatable strengthening aluminum alloy, and the mechanical properties of the ultra-high-strength alloy welded joints are predominantly controlled by the nano-scale precipitation characteristics across the SZ, TMAZ, HAZ, and BM. For peak-aged Al–Cu–Li alloys, a long-standing challenge arises from the intense thermal–mechanical cycle during FSW, which triggers severe dissolution, coarsening, and heterogeneous precipitation of strengthening precipitates, resulting in pronounced softening in the TMAZ and SZ. Conventional post-weld heat treatment (PWHT) strategies often fail to fully restore joint strength. The novelty of this study is to quantitatively reveal

the zone-resolved precipitation evolution under tailored PWHT and establish a definitive structure–property correlation, enabling a joint efficiency up to 95% via a newly developed solution + pre-stretching + aging route, which markedly outperforms conventional PWHT practices reported in the literature.

In the BM with T8 temper, high-density fine T_1 (Al_2CuLi) precipitates provide the dominant precipitation strengthening. During FSW, T_1 phases are almost completely dissolved in the SZ under severe plastic deformation and thermal cycling, followed by the precipitation of coarse AlCu, AlCuMg, and AlCuMn phases during cooling, leading to a sharp decrease in microhardness to approximately 140 HV. In the TMAZ, moderate thermal–mechanical input causes partial dissolution and coarsening of T_1, together with massive formation of coarse AlCu-based phases, giving rise to the lowest microhardness (~110 HV). The HAZ exhibits gradual softening toward the SZ due to T_1 coarsening. Consequently, the microhardness of the as-welded joint presents a typical "W"-shaped hardness profile. And the as-welded joint fractures in the TMAZ with an ultimate tensile strength (UTS) of 429 MPa and a joint efficiency of ~68%.

Direct artificial aging at 155 °C for 24 h produces no significant strengthening effect. Coarse secondary phases formed during welding consume abundant Cu, Li, and Mg solute atoms, reducing matrix supersaturation and eliminating the driving force for fine T_1 precipitation during aging. Pre-existing precipitates undergo further coarsening rather than refinement, leading to negligible changes in microhardness and tensile strength. These results confirm that single aging is ineffective for FSW joints of peak-aged Al–Cu–Li alloys.

Solution treatment at 515 °C for 2 h effectively re-dissolves coarse intermetallic phases into the matrix, restoring high supersaturation and reactivating the aging response. After subsequent aging, precipitates across all joint zones become highly uniform and are dominated by T_1 and θ' phases. The microhardness difference among zones is largely eliminated (~155 HV), and UTS increases to 504 MPa with a joint efficiency of ~80%. Although excellent microstructural homogeneity is achieved, joint strength is still limited by the relatively low fraction of T_1, the primary strengthening phase.

To further promote T_1 precipitation, pre-stretching deformation is introduced after solution treatment as the core innovation of this work. Pre-stretching generates high-density dislocations that serve as preferential nucleation sites for T_1, significantly increasing its number density and refining its size. With 3% pre-stretching, T_1 becomes the dominant strengthening phase in all zones, while θ' precipitation is greatly suppressed. Microhardness rises to ~185 HV, yield strength reaches 589 MPa, and UTS reaches 600 MPa, corresponding to a joint efficiency as high as 95%. This performance is superior to the published data for PWHT-treated FSW joints of third-generation Al–Li alloys. Typically, joint efficiencies of 75–85% are reported for FSW 2195-T8 joints after conventional aging or solution + aging, with few values exceeding 90% [32,34,35]. The 95% efficiency achieved herein demonstrates that pre-stretching-assisted PWHT can effectively repair FSW-induced strength loss and restore performance close to the BM level. The reduced elongation (1.81%) is associated with abnormal grain growth and intensified "S" line features in the SZ after the inclusion of a high-temperature solution, which act as a preferential fracture site. Further optimization of the solution's temperature, cooling rate, and pre-stretching level is suggested for applications requiring balanced strength and ductility.

Benchmarked against state-of-the-art literature, the solution + pre-stretching + aging route established in this study delivers a record-high joint efficiency compared with conventional aging, solution + aging, or rolling-assisted PWHT. Its key advantage lies in targeted precipitation control: pre-stretching maximizes the T_1 fraction and homogenizes its distribution across all zones, overcoming the inherent softening in the TMAZ and SZ that limits FSW joint performance. This work establishes a complete zone-resolved

structure–property relationship for PWHT of ultra-high-strength Al–Cu–Li FSW joints, providing reliable theoretical guidance and a practical processing route for high-performance aerospace structural components.

5. Conclusions

This present work employs a novel Al-Cu-Li alloy for friction stir welding. And the effects of post-welded heat treatment on microstructure and mechanical properties of joints were investigated. The following conclusions were obtained:

(1) The as-welded Al–Cu–Li alloy FSW joint exhibits a typical "W"-shaped microhardness distribution, with the lowest hardness in the TMAZ. The dissolution of T_1 strengthening phases and the precipitation of coarse AlCu, AlCuMg, and AlCuMn phases during FSW are identified as the primary reasons for joint softening.

(2) Direct post-weld aging at 155 °C for 24 h does not improve joint strength because coarse phases formed during welding consume abundant solute atoms and reduce the driving force for fine T_1 precipitation during aging.

(3) Solution treatment effectively re-dissolves coarse intermetallic phases, and subsequent aging homogenizes the microstructure across SZ, TMAZ, HAZ, and BM, with T_1 and θ' as the main strengthening phases.

(4) The solution + 3% pre-stretching + aging route represents the core innovation of this work. Pre-stretching introduces high-density dislocations to promote intensive nucleation of T_1 phases, which significantly enhances microhardness and tensile strength. The joint achieves an ultimate tensile strength of 600 MPa and a joint efficiency up to 95%, reaching an advanced level among the reported Al–Li alloy FSW joints.

Author Contributions: B.L.: conceptualization, methodology, software, investigation, resources, data curation, writing—original draft preparation; Y.L. (Ying Li): methodology, investigation, data curation, writing—review and editing; X.L.: conceptualization, investigation, writing—review and editing, project administration; Y.Z.: conceptualization, resources, writing—review and editing, project administration; K.W.: methodology, software, investigation, data curation, visualization; C.L.: methodology, software, investigation, visualization; L.Y.: methodology, formal analysis, investigation, data curation, writing—review and editing; Y.L. (Yanan Li): methodology, software, formal analysis, investigation, data curation; H.Y.: investigation, formal analysis, supervision, project administration; Z.L.: formal analysis, investigation, supervision, project administration; B.X.: formal analysis, investigation, supervision, project administration. All authors have read and agreed to the published version of the manuscript.

Funding: This research was funded by relevant national programs.

Data Availability Statement: The original contributions presented in this study are included in the article. Further inquiries can be directed to the corresponding authors.

Conflicts of Interest: Ben Lin was employed by China Academy of Launch Vehicle Technology, State Key Laboratory of Nonferrous Structural Materials, China GRINM Group Co., Ltd. and General Research Institute for Nonferrous Metals. Ying Li and Changlin Li were employed by State Key Laboratory of Nonferrous Structural Materials, China GRINM Group Co., Ltd. and GRIMAT Engineering Institute Co., Ltd. Zhihui Li and Baiqing Xiong were employed by State Key Laboratory of Nonferrous Structural Materials, China GRINM Group Co., Ltd. and General Research Institute for Nonferrous Metals. Xiwu Li, Yongan Zhang, Kai Wen, Lizhen Yan, Yanan Li and Hongwei Yan were employed by State Key Laboratory of Nonferrous Structural Materials, China GRINM Group Co., Ltd., General Research Institute for Nonferrous Metals and GRIMAT Engineering Institute Co., Ltd. The remaining authors declare that the research was conducted in the absence of any commercial or financial relationships that could be construed as a potential conflict of interest.

References

1. Williams, J.C.; Starke, E.A. Progress in structural materials for aerospace systems. *Acta Mater.* **2003**, *51*, 5775–5799. [CrossRef]
2. Zeng, X.; Wu, G.; Tong, X.; Li, L.; Xiong, X.; Zhang, L.; Qi, F.; Xu, X.; Guo, Y. Optimizing recrystallization behavior induced by Mn micro-alloying for reduced anisotropy in rolled Al–Cu–Li alloys. *Mater. Sci. Eng. A* **2024**, *909*, 146831. [CrossRef]
3. Braga, D.F.O.; Tavares, S.M.O.; da Silva, L.F.M.; Moreira, P.M.G.P.; Tavares de Castro, P.M.S. Advanced design for lightweight structures: Review and prospects. *Prog. Aerosp. Sci.* **2014**, *69*, 29–39. [CrossRef]
4. Xu, X.; Wu, G.; Tong, X.; Zhang, L.; Wang, C.; Qi, F.; Zeng, X.; Guo, Y. Achieving superior strength-ductility balance by tailoring dislocation density and shearable GP zone of extruded Al-Cu-Li alloy. *Int. J. Plast.* **2024**, *182*, 104135. [CrossRef]
5. Gupta, R.K.; Nayan, N.; Nagasireesha, G.; Sharma, S.C. Development and characterization of Al–Li alloys. *Mater. Sci. Eng. A* **2006**, *420*, 228–234. [CrossRef]
6. Tayon, W.A.; Nygren, K.E.; Crooks, R.E.; Pagan, D.C. In-situ study of planar slip in a commercial aluminum-lithium alloy using high energy X-ray diffraction microscopy. *Acta Mater.* **2019**, *173*, 231–241. [CrossRef]
7. Rioja, R.J.; Liu, J. The evolution of Al–Li base products for aerospace and space applications. *Metall. Mater. Trans. A* **2012**, *43*, 3325–3337. [CrossRef]
8. Feng, Y.; Chen, X.; Hao, Y.; Li, X.; Chen, B. Coarsening mechanism of T1 precipitation and calculation of T1/Al interface properties in 2198 Al–Cu–Li alloys: Experimental and DFT studies. *Vacuum* **2022**, *204*, 111333. [CrossRef]
9. Chen, Y.; Kong, F.; Yang, J.; Song, X.; Meng, X. Damage behavior of 2198-T8 Al–Li alloy with different corrosion fatigue modes. *Int. J. Fatigue* **2022**, *156*, 106671. [CrossRef]
10. Examilioti, T.N.; Li, W.; Kashaev, N.; Ventzke, V.; Klusemann, B.; Tiryakioğlu, M.; Alexopoulos, N.D. On anisotropic tensile mechanical behavior of Al–Cu–Li AA2198 alloy under different ageing conditions. *J. Mater. Res. Technol.* **2023**, *24*, 895–908. [CrossRef]
11. Abd El-Aty, A.; Xu, Y.; Guo, X.; Zhang, S.-H.; Ma, Y.; Chen, D. Strengthening mechanisms, deformation behavior, and anisotropic mechanical properties of Al–Li alloys: A review. *J. Adv. Res.* **2018**, *10*, 49–67. [CrossRef]
12. Lee, M.; Huang, J.; Ho, N. Microstructural and mechanical characterization of laser-beam welding of a 8090 Al–Li thin sheet. *J. Mater. Sci.* **1996**, *31*, 1455–1468. [CrossRef]
13. Shao, S.; Liang, Z.; Yin, P.; Li, X.; Zhang, Y. Microstructure and mechanical properties of Al–Li alloys with different Li contents prepared by selective laser melting. *Materials* **2024**, *17*, 657. [CrossRef]
14. Zhao, Y.; Li, X.; Liu, Z.; Wang, J.; Li, Y.; Zhan, X. Stability enhancement of molten pool and keyhole for 2195 Al–Li alloy using fiber-diode laser hybrid welding. *J. Manuf. Process.* **2023**, *85*, 724–741. [CrossRef]
15. Chen, D.; Zhan, X.; Liu, T.; Zhao, Y.; Qi, N.; Sun, L. Effect of porosity morphology and elements characteristics on mechanical property in T-joints during dual laser-beam bilateral synchronous welding of 2060/2099 Al–Li alloys. *Opt. Laser Technol.* **2021**, *140*, 107019. [CrossRef]
16. Enz, J.; Carrarin, C.; Riekehr, S.; Ventzke, V.; Kashaev, N. Hot cracking behaviour of an autogenously laser welded Al–Cu–Li alloy. *Int. J. Adv. Manuf. Technol.* **2017**, *95*, 299–310. [CrossRef]
17. Huang, Y.; Liu, P.-l.; Xiang, H.; Deng, S.-x.; Guo, Y.-j.; Li, J.-f. Mechanical properties, corrosion and microstructure distribution of a 2195-T8 Al–Li alloy TIG welded joint. *J. Manuf. Process.* **2023**, *90*, 151–165. [CrossRef]
18. Li, Q.; Wang, Q.; Xu, Y.; Sun, P.; Wang, K.; Tong, X.; Wu, G.; Zhang, L.; Xu, Y.; Ding, W. Welding of advanced aluminum–lithium alloys: Weldability, processing technologies, and grain structure control. *Materials* **2026**, *19*, 738. [CrossRef]
19. Sun, G.D.; Sun, W.Z.; Zhou, L. Microstructure, mechanical and fracture properties of friction stir welded 2195 Al–Li alloy joints. *Chin. J. Aeronaut.* **2024**, *37*, 345–361. [CrossRef]
20. Feddal, I.; Chairi, M.; Di Bella, G. Analysis of friction stir welding of aluminum alloys. *Metals* **2025**, *15*, 532. [CrossRef]
21. Yadav, A.K.; Trivedi, S.; Yadava, M.; Nayan, N.; Gurao, N.P. Determination of local constitutive behavior in friction stirred Al–Cu-Li alloy. *Mater. Today Commun.* **2025**, *46*, 112887. [CrossRef]
22. Wu, B.; Cheng, Q.; Zhao, H.; Zhang, H.; Miao, J.; Wang, Y.; Zhao, Y. Characteristics and mechanism of ultrasonic-assisted friction stir welding of aluminum lithium alloy. *J. Mater. Eng. Perform.* **2025**, *35*, 10697–10714. [CrossRef]
23. Chen, P.; Chen, J.; Qin, S.; Zou, S.; Song, S.; Jiang, T.; Zhang, Z.; Jia, Z.; Liu, Q. Friction stir welding joints of 2195-T8 Al–Li alloys: Correlation of temperature evolution, microstructure and mechanical properties. *Mater. Sci. Eng. A* **2021**, *823*, 141501. [CrossRef]
24. Kesharwani, G.S.; Billa, K.K.; Verma, J.; Garg, S.K.; Katiyar, J.K.; Kumar, S. Influence of tool velocity ratio on force-torque and mechanical properties of friction stir welded 2050-T84 Al–Li alloy plates. *Phys. Scr.* **2024**, *99*, 075008. [CrossRef]
25. Dai, X.; Shi, L.; Tian, C.-y.; Wu, C.-s.; Gao, S. Effect of ultrasonic vibration on microstructures and mechanical properties of friction stir welded 2195 Al−Li alloy. *Trans. Nonferrous Met. Soc. China* **2024**, *34*, 80–93. [CrossRef]
26. Lu, X.; Jiang, C.; Teng, L.; Shi, W.; Liang, S.Y. Prediction of the temperature distribution during friction stir welding 2195 Al–Li alloys. *J. Braz. Soc. Mech. Sci. Eng.* **2025**, *48*, 49. [CrossRef]
27. Lyu, X.; Zhang, X.; Shi, L.; Chen, J.; Wu, C. Elucidating the influence mechanisms of splat cooling on microstructure evolution in friction stir welding of 2195 Al–Li alloy by multi-scale simulation. *J. Mater. Res. Technol.* **2024**, *31*, 2636–2645. [CrossRef]

28. Lyu, X.; Tian, C.; Zhang, W.; Shi, L.; Wu, C.; Chen, J.; Yu, P. Revealing the mechanism of superimposing ultrasonic vibration on microstructure evolution in friction stir welding by multi-physical multi-scale simulation. *J. Manuf. Process.* **2024**, *124*, 300–315. [CrossRef]
29. Tong, Y.; Dong, B.; Cai, X.; Zhang, H.; Lin, S. Friction stir welding of 2195 Al–Li alloy: Effect of microstructure on joint failure. *Mater. Charact.* **2025**, *224*, 115077. [CrossRef]
30. Thomas, B.; Sreejith, P.S. Microstructural analysis and process parameter optimization of friction stir-welded AA8090 alloys for enhanced tensile strength. *Mater. Res. Express* **2025**, *12*, 106509. [CrossRef]
31. Shao, M.; Huang, C.; Chang, X.; Zhou, A.; Wang, Y. Microstructural evolution, deformation behaviour and corrosion properties of 2195 Al–Li alloy friction stir welding T-junction. *J. Alloys Compd.* **2025**, *1012*, 178504. [CrossRef]
32. Chen, P.; Chen, W.; Wang, J.; Zhang, J.; Tang, Y.; Huang, B.; Zhang, Z. Enhancing mechanical properties of friction stir welded 2195-O Al–Li alloys by post-weld heat treatment. *Mater. Charact.* **2025**, *227*, 115219. [CrossRef]
33. Wang, D.; Zhan, L.; Liu, C.; He, D.; Lai, R.; Li, Y.; Zeng, Q.; Huang, M. Effect of temperature on creep aging behavior of the nugget zone of AA2195 Al–Li alloy produced by friction stir welding. *Mater. Charact.* **2024**, *217*, 114408. [CrossRef]
34. Chen, P.; Wang, J.; Liu, G.; Chen, W.; Tang, Y.; Huang, B.; Zhang, Z. Influence of post-weld rolling and artificial aging on microstructure and mechanical properties of friction stir welded 2195-T4 Al–Li alloy joints. *Mater. Sci. Eng. A* **2024**, *914*, 147165. [CrossRef]
35. Chen, J.; Chen, R.; Liao, H.; He, Y.; Chen, P.; Tian, Y.; Zhang, B.; Zhang, Z. Improving joint performance of friction stir welded 2195-O Al–Li alloy by post-weld heat treatment and rolling deformation. *J. Mater. Res. Technol.* **2024**, *29*, 5048–5059. [CrossRef]
36. *ASTM E384-22*; Standard Test Method for Microindentation Hardness of Materials. ASTM International: West Conshohocken, PA, USA, 2022.
37. *ASTM E8-04*; Standard Test Methods for Tension Testing of Metallic Materials. ASTM International: West Conshohocken, PA, USA, 2004.
38. Charit, I.; Mishra, R.S. Abnormal grain growth in friction stir processed alloys. *Scr. Mater.* **2008**, *58*, 367–371. [CrossRef]

Disclaimer/Publisher's Note: The statements, opinions and data contained in all publications are solely those of the individual author(s) and contributor(s) and not of MDPI and/or the editor(s). MDPI and/or the editor(s) disclaim responsibility for any injury to people or property resulting from any ideas, methods, instructions or products referred to in the content.